Large eddy simulation study of scalar transport in fully developed wind-turbine array boundary layers

Marc Calaf, Marc B. Parlange, and Charles Meneveau

Related Articles

Mechanical stability of ordered droplet packings in microfluidic channels
Appl. Phys. Lett. 99, 244104 (2011)

Numerical investigation and evaluation of optimum hydrodynamic performance of a horizontal axis hydrokinetic turbine
J. Renewable Sustainable Energy 3, 063105 (2011)

Microscale pH regulation by splitting water
Biomicrofluidics 5, 046502 (2011)

Curvature-induced secondary microflow motion in steady electro-osmotic transport with hydrodynamic slippage effect
Phys. Fluids 23, 102004 (2011)

Drag reduction of a hairy disk
Phys. Fluids 23, 101701 (2011)

Additional information on Phys. Fluids

Journal Homepage: http://pof.aip.org/

Journal Information: http://pof.aip.org/about/about_the_journal

Top downloads: http://pof.aip.org/features/most_downloaded

Information for Authors: http://pof.aip.org/authors

Large eddy simulation study of scalar transport in fully developed wind-turbine array boundary layers

Marc Calaf,[1,a)] Marc B. Parlange,[1,b)] and Charles Meneveau[2,c)]

[1]*School of Architecture, Civil and Environmental Engineering, École Polytechnique Fédérale de Lausanne (EPFL), 1015 Lausanne, Switzerland*
[2]*Department of Mechanical Engineering, Johns Hopkins University, 3400 North Charles Street, Baltimore, Maryland 21218, USA*

Wind harvesting is fast becoming an important alternative source of energy. As wind farms become larger, they begin to attain scales at which two-way interactions with the atmospheric boundary layer (ABL) must be taken into account. Several studies have shown that there is a quantifiable effect of wind farms on the local meteorology, mainly through changes in the land-atmosphere fluxes of heat and moisture. In particular, the observed trends suggest that wind farms increase fluxes at the surface and this could be due to increased turbulence in the wakes. Conversely, simulations and laboratory experiments show that underneath wind farms, the friction velocity is decreased due to extraction of momentum by the wind turbines, a factor that could decrease scalar fluxes at the surface. In order to study this issue in more detail, a suite of large eddy simulations of an infinite (fully developed) wind turbine array boundary layer, including scalar transport from the ground surface without stratification, is performed. Results show an overall increase in the scalar fluxes of about 10%–15% when wind turbines are present in the ABL, and that the increase does not strongly depend upon wind farm loading as described by the turbines' thrust coefficient and the wind turbines spacings. A single-column analysis including scalar transport shows that the presence of wind farms can be expected to increase slightly the scalar transport from the bottom surface and that this slight increase is due to a delicate balance between two strong opposing trends. © 2011 American Institute of Physics. [doi:10.1063/1.3663376]

I. INTRODUCTION

As wind energy emerges as the fastest and most robustly growing form of renewable energy, wind farms are increasing in size and numbers. Large wind farms begin to attain scales at which interactions with the atmospheric boundary layer (ABL) must be taken into account, not only in how the ABL wind affects power output but also how a wind farm affects the local meteorology and downstream wind farms. In pioneering work, Baidya-Roy *et al.*[1] numerically studied the potential impact of large wind farms on mesoscale ABL processes. Baidya-Roy and Traiteur[2] repeated such analysis using data obtained from the San Gorgonio Pass wind farm. Both analyses showed that due to an increase in turbulent mixing in the wind farm, the surface temperature was modified depending on the atmospheric stratification. The results suggested in general increasing surface fluxes due to the wind farm. Changes of surface latent heat fluxes (and of other scalars) due to wind farms is an important issue also for climate and weather simulations at larger scales.[3,4]

Recently, Calaf *et al.*[5] used more detailed large eddy simulations (LES) in a micrometeorological setting to study the momentum and kinetic energy fluxes taking place inside wind farms. Averages were performed over horizontal planes leading to vertical profiles of mean velocity, Reynolds stresses, and kinetic energy fluxes. The simulations show that a region of enhanced momentum transport is created above the wind turbine region (increased friction velocity), while a reduction of momentum flux (reduced friction velocity) occurs underneath the wind turbines. Similar trends were obtained in wind tunnel measurements.[6] As a consequence of these results, a new question is raised: Given that the momentum flux close to the ground has been shown to be attenuated, do the surface scalar fluxes decrease rather than increase, in the presence of wind turbines? The present paper attempts to shed light on this issue by performing LES of wind farms including scalar transport.

As further background, it can be recalled that from a mechanical perspective, much research has already been done on wind blade aerodynamics and single wind turbine optimization for maximal power extraction.[7,8] Also, the wake structure of a single wind turbine is a fairly well explored topic,[9–18] together with superposition effects of a finite number of wakes and their mutual interactions.[19–25] Pioneering works of Lissaman[26] and later Frandsen[25] led the way for understanding and modeling of an "infinite," or fully developed, array of wind turbines. The ABL across a landscape patch may be considered fully developed when the length of the patch is much larger than its height,[27] length $\gg 10 \times$ height. Therefore, wind farms greater than 10–20 km can be considered as approaching a fully developed regime, for a characteristic ABL height of 1 km. It is possible then to define a wind turbine array boundary layer (WTABL), where the flow is fully developed. Such a concept was implicitly assumed in the

aforementioned simulations of Baidya-Roy *et al.*,[1] Keith *et al.*,[3] and Barrie and Kirk-Davidoff.[4] Both Keith *et al.*[3] and Barrie and Kirk-Davidoff[4] parameterized wind turbines by means of an induced surface roughness, with the assumption of "fully developed" flow being implicit due to their grid resolution. Baidya-Roy *et al.*[1] also used a meso-scale model with wind turbines being parameterized as a sink of energy and a source of turbulence. Therefore, the notion of a fully developed WTABL has gained interest from various points of view. The LES results of Calaf *et al.*[5] for a fully developed WTABL were analyzed to derive a new parameterization for the induced wind farm surface roughness, as a generalization of an earlier model by Frandsen[25] and Frandsen *et al.*,[28] now including the additional mixing due to the wind turbine wake region. While evidently quite a bit of knowledge exists about wind farms, the aforementioned competing mechanisms determining whether wind farms increase or decrease surface fluxes of scalars remain to be addressed in detail.

As in Calaf *et al.*,[5] the current study is based on LES. The LES code uses periodic boundary conditions in the horizontal directions allowing for a nominally infinite wind farm, consistent with the asymptotic regime of a fully developed WTABL. The simulation uses sufficient numerical resolution so that a coarse representation of individual wind turbine disks is possible. This allows us to carry out a detailed analysis of the scalar (heat) flux formation and interaction with wind turbines. Similar to Calaf *et al.*,[5] the flow is driven by an imposed pressure gradient, and the vertical dimension of the domain (e.g., $H = 1000$ m) is such to be representative of the ABL height. The use of pressure gradient forcing allows us to ensure that the mean flow is perpendicular to the wind turbine disk, and the notion of inner flow and outer flow separation allows us to assume that the results to be obtained will also be relevant to the more realistic scenario of flow driven by an external geostrophic wind (see discussion in the Appendix of Calaf *et al.*[5]). In order to characterize scalar fluxes in response to various strengths of wind farm "loading," several different wind turbine parameters such as the thrust coefficient and the stream-wise and span-wise turbine spacings will be considered in a suite of LES cases. And, to first focus only on scalar transport without additional effects of buoyancy, in this paper, we consider the case of passive scalar in a neutral ABL.

The LES technique used is described in Sec. II, with the cases considered and parameters chosen for the simulations summarized in Sec. II C. Results are presented in Sec. III, where some representative instantaneous distributions are shown, together with mean velocity, total shear stress, and scalar flux profiles. The simulations are analyzed with the specific aim to determine whether surface scalar fluxes increase or decrease in the presence of wind farm and to identify any trends with respect to the wind farm parameters. In order to better understand the observed trends, a 1-D analysis of vertical scalar flux is performed in Sec. IV, following the approach in Calaf *et al.*[5] Results comparing this model and the LES results are presented in Sec. V. The conclusions are summarized in Sec. VI.

II. LARGE EDDY SIMULATION METHODOLOGY AND CASES

A. Governing equations and LES code

Simulations of a pressure-gradient driven, fully developed boundary layer flow with a passive scalar are performed. The large eddy simulation code used in this study solves the non-dimensional filtered incompressible Navier-Stokes (NS) equations with the continuity constraint for the momentum, and the advection-diffusion equation for the scalar field, θ, i.e.,

$$\partial_i \tilde{u}_i = 0, \tag{1}$$

$$\partial_t \tilde{u}_i + \partial_j (\tilde{u}_i \tilde{u}_j) = -\partial_i \tilde{p}^* - \partial_j \tau_{ij} + f_i - \delta_{i1} \partial_1 p_\infty / \rho, \tag{2}$$

$$\partial_t \tilde{\theta} + \tilde{u}_i (\partial_i \tilde{\theta}) = -\partial_i r_i, \tag{3}$$

with $\widetilde{u}_i$ and $\widetilde{\theta}$ being the filtered velocity field and passive scalar field (e.g., temperature), respectively. Also, $\tilde{p}^*$ is the filtered modified pressure divided by density which is equal to $\tilde{p}/\rho + \tau_{kk}/3 - p_\infty/\rho$. τ_{ij} is the trace free $(\tau_{ij} - \delta_{ij}\tau_{kk}/3)$ subgrid-scale (SGS) stress tensor that it is modeled using the Lagrangian scale-dependent model of Bou-Zeid *et al.*[29] Its trace $(\tau_{kk}/3)$ is included into the modified pressure, as is common practice in incompressible LES. Further, r_i is the SGS flux of the scalar field which is modeled using a dynamic scale-dependent eddy-diffusion approach, similar to that used for the subgrid-scale stress term (its derivation is presented in the Appendix). Finally, f_i models the effect of the wind turbines in the flow (see Sec. II B). Because we are considering an atmospheric flow and, therefore, the Reynolds number is high, the molecular viscous and diffusive effects are neglected.

Real ABL flows are driven by a geostrophic forcing, where the outer layer is affected by Coriolis accelerations, making the flow turn near the ground. For the sake of simplicity, we force a mean flow perpendicular to the wind turbine disks using an imposed pressure gradient, $\partial_1 p_\infty$, in the x_1 direction. However, the simulation results especially in the surface layer region can still be interpreted in the context of geostrophic wind forcing, as summarized in the Appendix of Calaf *et al.*[5]

Following the approach of Moeng,[30] Albertson and Parlange,[27] Albertson and Parlange,[31] and Porté-Agel *et al.*,[32] the numerical scheme solves the skew-symmetric form of the NS equation using a pseudo-spectral discretization in the horizontal directions and second order finite differences in the vertical direction. The second order accurate Adams–Bashforth scheme is used for time advancement. Also, the non-linear convective terms in both the momentum and scalar equations are de-aliased with the 3/2 rule.[33] Message passing interface (MPI) is used to parallelize the code, and the (Fastest Fourier Transform in the West) FFTW library[34] is used for high performance fast Fourier transform evaluations.

At the top boundary, at height $z = H$, a zero vertical velocity and zero shear stress boundary condition for the momentum, together with a small and constant vertical scalar derivative $(d\theta/d(z/H)|_{top} = 6)$ are imposed. At the bottom surface, the wall stress is imposed using the standard log (Monin-Obukhov) similarity law[30]

$$\tau_{w1} = -\left(\frac{\kappa}{\ln z_1/z_{0,lo}}\right)^2 \left(\widehat{\hat{u}}^2 + \widehat{\hat{v}}^2\right)^{0.5} \widehat{\hat{u}}, \qquad (4)$$

$$\tau_{w2} = -\left(\frac{\kappa}{\ln z_1/z_{0,lo}}\right)^2 \left(\widehat{\hat{u}}^2 + \widehat{\hat{v}}^2\right)^{0.5} \widehat{\hat{v}}, \qquad (5)$$

where the hat on $\hat{u}$ and $\hat{v}$ represents a local average obtained by filtering the LES velocity field with filter width 2Δ (see Bou-Zeid *et al.*[29] for more details about such filtering). These velocities are evaluated on the first gridpoint at a height $z_1 = \Delta z/2$, where Δz is the vertical grid spacing (the code uses staggered grids in the vertical direction). The surface roughness ($z_{0,lo} = 10^{-4}H$) is kept constant, and κ is the Von Kármán constant ($\kappa = 0.4$). For the scalar, a fixed value at the surface (θ_s) is imposed. The corresponding passive scalar flux q_s at the surface is computed with Monin-Obukhov similarity theory

$$q_s(x,y) = \frac{\kappa^2 [\theta_s - \tilde{\theta}(x,y,z_1)] \sqrt{\hat{\tilde{u}}^2 + \hat{\tilde{v}}^2}}{\ln\left(\frac{z_1}{z_{0,s}}\right) \ln\left(\frac{z_1}{z_{0,lo}}\right)} \qquad (6)$$

where the scalar surface roughness is prescribed as $z_{0,s} = z_{0,lo}/10 = 10^{-5}H$. The applied pressure gradient $\partial_1 p_\infty/\rho$ defines a reference, fixed friction velocity u_{*hi} by means of $u_{*hi}^2 = H\partial_1 p_\infty/\rho$. This, in turn, is directly linked to an external geostrophic wind speed,[35]

$$U_G = \frac{u_{*hi}}{\kappa}\left[ln\left(\frac{U_G}{fz_{0,hi}}\right) - C_*\right] = \frac{u_{*hi}}{\kappa}\left[ln\left(Ro_h \frac{z_h}{z_{0,hi}}\right) - C_*\right], \qquad (7)$$

where the empirical coefficient $C_* = 4$ is known from the prior literature,[28] and $Ro_h = U_G/(fz_h)$ is the hub-height Rossby number. Also, $z_{0,hi}$ is the effective roughness length that will result from average behavior of the flow above the wind farm. Since for any given prescribed pressure gradient (or prescribed u_{*hi}), different wind farm arrangements will lead to different effective roughness $z_{0,hi}$ (Ref. [5]), the ratio u_{*hi}/U_G will differ for each of the cases. Therefore, care must be taken to scale velocities with the variable that for a real wind farm would be "externally imposed," namely, the geostrophic wind U_G. Specifically, velocities will be scaled with U_G, as obtained using Eq. (7) for any given $z_{0,hi}$ and specified value of the Rossby number. As a reference, in this paper, we use $Ro_h = 1000$, which corresponds to $U_G = 10$ m/s, $z_h = 100$ m and mid-latitude frequency of $f = 10^{-4}$ s^{-1}. Further, scalar fluxes arising in the simulations will be normalized with the geostrophic velocity U_G and the scalar difference $(\theta_s - \theta_\infty)$. The scalar concentration $(\theta_s - \bar{\theta}(z))$ is normalized with the overall scalar difference $(\theta_s - \theta_\infty)$ across the entire domain at any given time, where θ_s is the fixed scalar at the surface and $\theta_\infty \equiv \bar{\theta}(H)$ is the scalar value at the top of the domain. The latter value evolves slowly in time. Since each wind farm case mixes and entrains scalar at different time rates, it is important to normalize the heat flux at the surface with the overall scalar difference that drives the scalar flux at a given time in order to obtain values that can be compared across different cases.

B. Wind turbine model

The wind turbines are modeled through an actuator (drag) disk approach. This approach has already been used in past studies.[5,36,37] In particular, the detailed comparisons with wind tunnel data presented in Wu and Porté-Agel[38] show that except for the near-wake region, the drag disk approach yields a good degree of accuracy. The method is based on a drag force (F_t) acting in the stream-wise direction (x_1) according to

$$F_t = -\frac{1}{2}\rho C_T U_\infty^2 \frac{\pi}{4}D^2, \qquad (8)$$

where C_T is the thrust coefficient, D is the rotor diameter, and U_∞ is an upstream (unperturbed) velocity. This is a good approach when one is modeling a single wind turbine[36,37] and there are no other interacting bodies in the numerical domain that can make specification of U_∞ ambiguous. When modeling wind farms, it is impossible to define an unperturbed upstream mean velocity since the upstream values are always affected by other upstream wind turbines.[39] It is thus more convenient to use the local velocity at the rotor disk U_d.[5,39] It can be related to an equivalent upstream unperturbed velocity through the actuator-disk theory

$$U_\infty = \frac{U_d}{(1-a)}, \qquad (9)$$

where a is the induction factor.[8] Also, instead of the local velocity at each grid-point, an average disk velocity[39] is needed for modeling the thrust forces acting on the fluid due to its interaction with the rotating blades. Therefore, in the LES, the local disk velocity is averaged over the disk and also over a short period of time ($\langle \bar{u}^T \rangle_d$), so that the thrust force is given by

$$F_t = -\rho \frac{1}{2} C_T' \langle \bar{u}^T \rangle_d^2 \frac{\pi}{4}D^2, \qquad (10)$$

where $\langle \rangle_d$ means averaging over the rotor disk, and $\bar{u}^T$ refers to averaging over a time-scale T. The disk averaged velocity is obtained by spatial averaging over all grid points inside the disk, and the temporal average is done using a one-sided exponential time-filter (first order relaxation process) over a time-period T, given in dimensionless form as $Tu_{*hi}/H = 0.27$. We also define

$$C_T' = \frac{C_T}{(1-a)^2}, \qquad (11)$$

and we characterize the overall wind farm loading using the planform loading factor $c_{ft} = \pi C_T/(4s_x s_y)$ or $c_{ft}' = \pi C_T'/(4s_x s_y)$ through most of the analysis. Using typical values $C_T = 0.75$, and $a = 1/4$, found in existing wind-turbines[8] and prior LES study,[36] leads to a nominal value of $C_T' = 4/3$. As reference, the Betz limit[8] case (i.e., $C_T = 8/9$ and $a = 1/3$) leads to $C_T' = 2$. In this study, different thrust coefficients (C_T) and wind turbines spacings ($s_x D$ in streamwise direction and $s_y D$ in spanwise direction) have been considered, leading to a range of loading factors c_{ft}.

The total thrust force is distributed evenly across the various grid points that fall inside the wind turbine disk region. This region has a thickness of a grid cell in the stream-wise direction, and in the cross-vertical direction spans through different grid cells according to the wind turbine's diameter (D) and the hub (rotor disk center) location. The force is distributed over the different grid cells proportionally to its frontal area coinciding with the wind turbine's disk, i.e., $\gamma_{j,k}\Delta y\Delta z$, where $\gamma_{j,k}$ is the fraction of area overlap between the cell at grid-point (j, k) (position y_j, z_k) and the circle. For cells that are completely submerged inside the wind turbine's disk, $\gamma_{j,k} = 1$. For cells that are fully outside the wind turbine's rotor disk, $\gamma_{j,k} = 0$. And for those cells that partially overlap with the rotor disk, $\gamma_{j,k}$ corresponds to a factor proportional to the overlapping area.

Finally, the thrust force per unit mass at position (x_i, y_j, z_k) is re-written as follows:

$$f_1(x_i, y_j, z_k) = -\frac{1}{2}C_T'\langle\bar{u}^T\rangle_d^2\frac{\gamma_{j,k}}{\Delta x}. \tag{12}$$

C. Suite of LES cases

In the simulations, the number of wind turbines (N_t), the distances among them (s_xD and s_yD), and the relative sparseness of their distribution ($S/A = 4s_xs_y/\pi$), together with the thrust coefficient C_T', that represents the loading of each wind turbine, are varied. The wind turbines rotor diameter are equal among all wind turbines and all wind farm configurations ($D = 100$ m). Also the numerical resolution is kept constant (given by the parameters $L_x, L_y, L_z = (\pi, \pi, 1)H$ and $N_x, N_y, N_z = 128$) and the grid spacing is uniform in all three directions. The suite of LES cases is described in Table I. The wind turbine loading is changed from a very weak scenario (case A, $C_T' = 0.6$), up to a scenario matching the Betz limit (case G, $C_T' = 2$). Further, the loading is also increased by changing the physical arrangement of the wind turbines, where the reference spacings ($s_{x0} = 7.85$, $s_{y0} = s_{x0}/1.5$) have been modified. Three cases are studied: ($s_{x0}/2, s_{y0}$), ($s_{x0}, s_{y0}/2$), ($s_{x0}/2, s_{y0}/2$), where the thrust coefficient is kept fixed ($C_T' = 1.33$). The same physical domain is considered in all cases, with a fixed surface roughness $z_{0,lo}/H = 10^{-4}$, and a scalar surface roughness that is 10% of the momentum roughness scale, $z_{0,s}/H = 10^{-5}$.

TABLE I. Table summarizing parameters of the various LES cases.

	s_x	s_y	$4s_xs_y/\pi$	N_t	C_T	C_T'	c_{ft}	c_{ft}'
A	7.85	$s_x/1.5$	52.3	4×6	0.45	0.6	0.009	0.011
B	7.85	$s_x/1.5$	52.3	4×6	0.52	0.7	0.01	0.013
C	7.85	$s_x/1.5$	52.3	4×6	0.6	0.88	0.012	0.017
D	7.85	$s_x/1.5$	52.3	4×6	0.68	1.13	0.013	0.022
E	7.85	$s_x/1.5$	52.3	4×6	0.75	1.33	0.014	0.025
F	7.85	$s_x/1.5$	52.3	4×6	0.82	1.63	0.016	0.031
G	7.85	$s_x/1.5$	52.3	4×6	0.88	2	0.017	0.038
E1	7.85/2	7.85/1.5	26.15	8×6	0.75	1.33	0.029	0.051
E2	7.85	$s_x/3$	26.15	4×12	0.75	1.33	0.029	0.051
E3	7.85/2	$s_x/1.5$	13.1	8×12	0.75	1.33	0.057	0.1

Simulations are initialized with a vertical logarithmic profile with added random noise for the $\tilde{u}_1$ component, and zero mean value with added random noise for components $\tilde{u}_2$ and $\tilde{u}_3$. The scalar field is also initialized with a logarithmic profile with added random noise. All cases are run for 58.5 non-dimensional time units (where the dimensionless time is in units of H/u_{*hi}). Statistics are accumulated over the last 18 non-dimensional time units. After the first 40.5 non-dimensional time units, the different cases converge and statistical stationarity is achieved for the momentum variables as well as for the scalar.

Although the size of the domain, and the number of wind turbines (e.g., 4×6) in the simulation are not sufficient by themselves to allow a "fully developed" boundary layer to develop, the periodic boundary conditions and the long simulation times enable fully developed flow characteristics to be established. A sample of instantaneous contour plots is shown in Figs. 1(a) and 1(b). They show dimensionless streamwise velocity ($\tilde{u}/u_{*hi}$) and the passive scalar difference between the surface and hub-height normalized by the overall change in scalar across the boundary layer (($\theta_s - \tilde{\theta})/(\theta_s - \theta_\infty)$), in the horizontal x–y plane. The plane cuts through the wind turbine centers, and the position and extents of the wind turbine disks are indicated with black lines. It is interesting to remark the different behavior between scalar and momentum. The stream-wise velocity correlates more strongly with the locations of the rotor disks, showing the localized wakes. The scalar field, not being directly affected by the presence of the rotors and only indirectly through the transporting velocity field, shows a less organized behavior. Although wake effects are less clear in the scalar field, the correlation between high and low speed channels with high and low scalar difference regions is also clearly visible.

III. LARGE EDDY SIMULATION RESULTS

In Figure 2, the vertical profiles of the filtered mean stream-wise velocity normalized with the friction velocity u_{*hi} (imposed through the fixed pressure gradient) are shown, for all cases. The symbol $\langle\rangle$ implies averaging over the horizontal directions. To simplify notation, the LES filtering "tilde" will be omitted from the indicated variables. Following the approach described in Calaf *et al.*,[5] these results are used to determine the effective roughness height $z_{0,hi}$. Using the equation for the mean flow velocity $\langle u\rangle/u_{*hi} = 1/\kappa\ln(z/z_{0,hi})$ and because of the good logarithmic behavior of the data above the wind turbines, the effective surface roughness can be obtained from a single point value of the mean velocity, e.g., at twice the hub height ($z = 2z_h$) and using $\kappa = 0.4$,

$$z_{0,hi} = 2z_h\exp\left(-\frac{\kappa\langle u\rangle}{u_{*hi}}\right). \tag{13}$$

Further, the numerical results initially normalized by u_{*hi} are re-normalized by the factor u_{*hi}/U_G, computed using Eq. (7) for the fixed $Ro_h = 1000$. As consequence, the results can be compared meaningfully since they correspond to a common value of an imposed equivalent geostrophic wind velocity
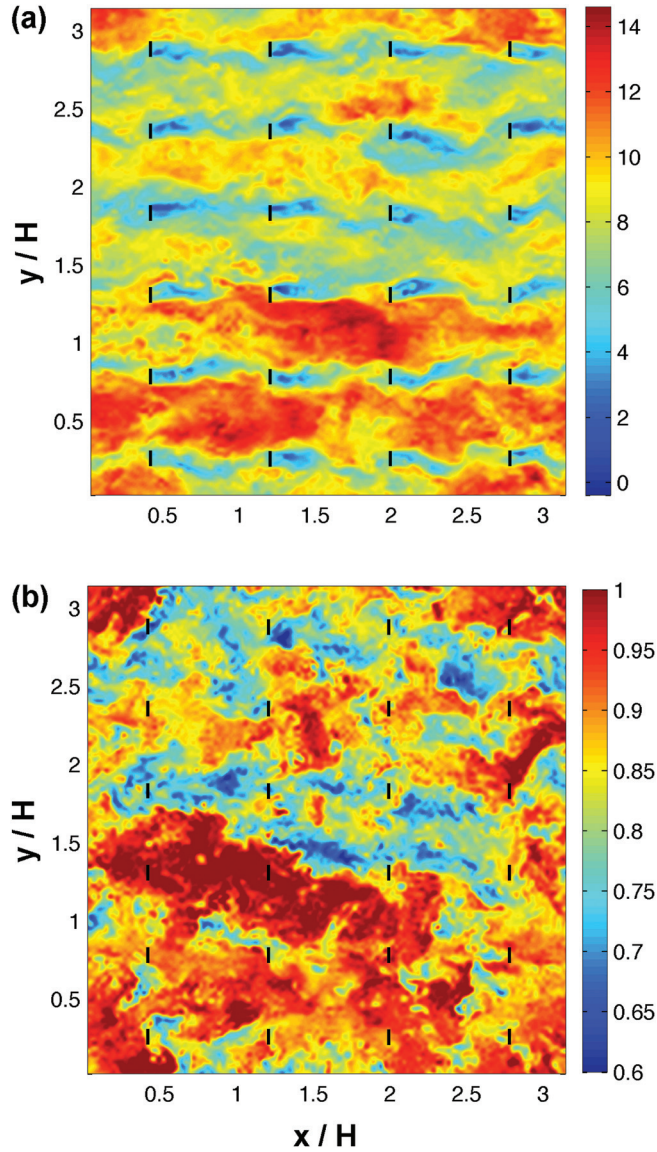
(a)

(b)

FIG. 1. (Color) Instantaneous contours of stream-wise velocity and scalar difference from LES of a fully developed wind turbine array boundary layer (case F); (a) stream-wise velocity $\tilde{u}_1/u_{*hi}$ on a x–y plane at a height $z = z_h$ corresponding to hub-height (the wind turbine centers). (b) Normalized scalar difference distribution $(\theta_s - \tilde{\theta})/(\theta_s - \theta_\infty)$, at the same x–y plane and the same time.
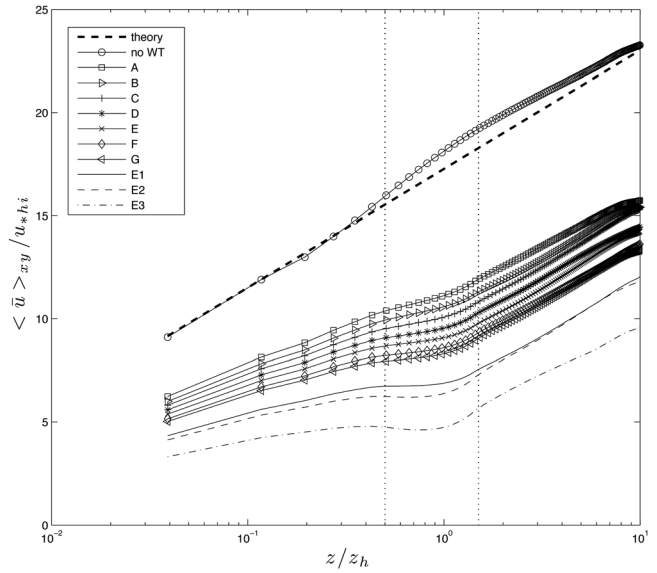

FIG. 2. Mean velocity profiles for wind farms with different loading parameters. The dotted straight line represents the theoretical logarithmic profile: $\langle \bar{u} \rangle / u_{*hi} = 1/\kappa \ln(z/z_0)$, and the solid line with hollow circles shows the LES result for the case with no wind turbines. The two parallel dotted lines represent the lower and upper limit of the wind turbine rotor disk. These will be used for the remainder of the vertical profile plots.

velocity is normalized by the nominally imposed U_G instead of friction velocity. The inner region of the profile below the wind turbine region is less perturbed, but a slight decrease in slope (proportional to u_{*lo}) is observed. By increasing the c_{ft} parameter (first by increasing C_T, and then by decreasing s_x and s_y), the mean wind speed across the layers is reduced progressively. For cases A to G, the mean wind speed at hub height shows a rather constant decrease. But when increasing the load through a reduction of s_x, s_y (cases E1-E3), the decrease of mean wind speed is much more pronounced (solid, dashed, and dotted-dashed lines in Figure 3).

Figure 4 shows vertical profiles of the total shear stress, τ_{xz}, defined as the sum of Reynolds, dispersive, and mean SGS stress,[5] according to

$$\tau_{xz}(z) = -\langle \overline{u'w'} \rangle(z) - \langle \bar{u}''\bar{w}'' \rangle(z) - \langle \tau_{xz}^{sgs} \rangle(z), \quad (14)$$

U_G. Table II summarizes the measured values of the effective surface roughness $z_{0,hi}$ for the different cases and the corresponding re-normalization factors computed using Eq. (7) using the measured $z_{0,hi}$. In Figure 3, the vertical profiles of the filtered mean stream-wise velocity once re-normalized with the geostrophic wind speed ($\langle \tilde{u} \rangle / U_G$) are presented. The dotted straight line represents the theoretical logarithmic profile: $\langle u \rangle / U_G = (u_*/\kappa U_G) \ln(z/z_{0,lo})$ appropriate for the case without wind turbines, and the solid line with hollow circles shows the LES result for the case with no wind turbines. It matches well the theoretical logarithmic profile in the inner boundary layer, which extends up to slightly above the hub height ($z/z_h \sim 1.5$). When introducing wind turbines, the outer logarithmic profile is affected by a significant increase in u_{*hi} (proportional to the slope of the logarithmic region above the wind turbines), since the mean

TABLE II. Table summarizing the measured effective surface roughness for the different study cases and the corresponding re-normalization factors u_{*hi}/U_G, computed using Eq. (7) for the fixed $Ro_h = 1000$.

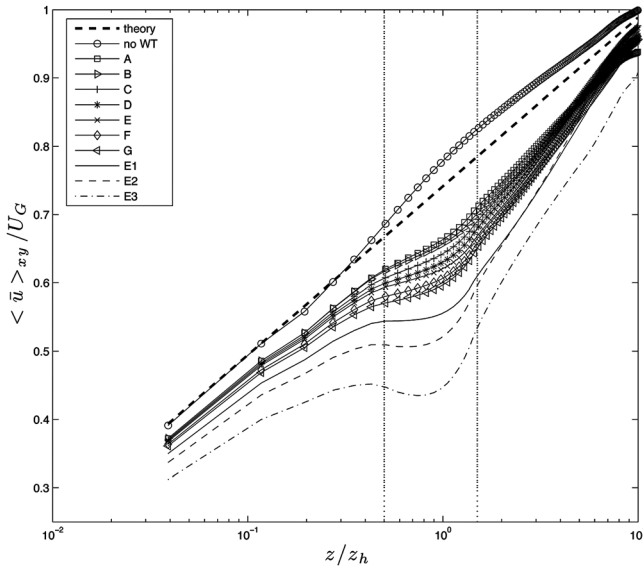|	$(z_{0,hi}/z_h)$	u_{*hi}/U_G
A	1.4×10^{-2}	0.06
B	1.8×10^{-2}	0.062
C	2.1×10^{-2}	0.064
D	2.6×10^{-2}	0.066
E	3.2×10^{-2}	0.068
F	3.8×10^{-2}	0.071
G	4.2×10^{-2}	0.072
$E1$	7.9×10^{-2}	0.081
$E2$	8.3×10^{-2}	0.082
$E3$	16×10^{-2}	0.094

FIG. 3. Mean velocity profiles for wind farms with different loading parameters. The dotted straight line represents the theoretical logarithmic profile: $\langle \bar{u} \rangle / U_G = (u_* / \kappa U_G) \ln(z/z_{0,lo})$, and the solid line with hollow circles shows the LES result for the case with no wind turbines.

where the dispersive stress arises due to the correlations among the spatially non-homogeneous mean horizontal and mean vertical velocity,[40] with u'' and w'' being defined as $\bar{u} - \langle \bar{u} \rangle$ and $\bar{w} - \langle \bar{w} \rangle$. The shear stress profiles all show the expected linear behavior (balancing the constant imposed pressure gradient), until close to the top of the wind turbine region (delimited by the horizontal dotted lines, between $z/z_h = 0.5$ and $z/z_h = 1.5$). In this region, the drag due to the turbines begins to deplete the momentum fluxes until below the wind turbine region. Figure 4(a) shows the profiles for cases A to G, where the thrust coefficient is changed. A progressive increase in the shear stress at $z/z_h = 1.5$, right above the wind turbine disk, is observed. Conversely, a progressive decrease in the shear stress at $z/z_h = 0.5$, underneath the wind turbine disk, is also observed. This decrease is less noticeable than the increase above the wind-turbine region. A zoom in this region is presented on the right, top corner of the figure. Figure 4(b) shows the same profiles but for cases E and E1-E3. Relevant is the increase in the shear stress above the wind-turbine region for case E3. For these cases (E), the decrease in shear stress underneath the wind-turbine disk is more pronounced. From these plots, we obtain values for u_{*hi} and u_{*lo} as follows:

$$u_{*hi} = \sqrt{\tau_{xz}(z_h + D/2)}, \quad u_{*lo} = \sqrt{\tau_{xz}(z_h - D/2)}. \quad (15)$$

The two friction velocities, as well as their ratio, are shown in Figure 5 as function of the loading parameter c_{ft}. The plot also shows a comparison with results from a 1D model (lines) to be reviewed in Sec. IV. The friction velocities are normalized with U_G, obtained as before for each loading case by evaluating the effective roughness length $z_{0,hi}$ from the LES and then replacing into Eq. (7) for $Ro_h = 1000$. As can be seen, as the loading increases, for a fixed imposed geostrophic velocity, the friction velocity above the wind farm increases significantly, whereas below the wind farm it
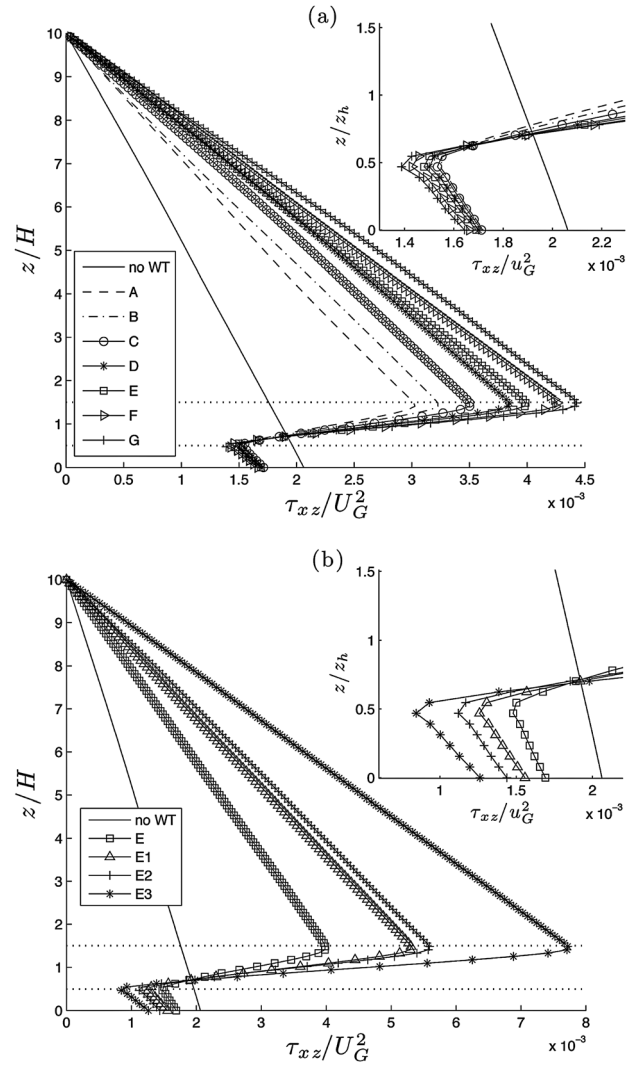

FIG. 4. Vertical profiles of the total shear stress for wind farms with different loading coefficients. (a) shows the profiles for cases A to G, where the thrust coefficient is changed. On the top, right corner, the lowest 15% of the bottom region of the shear stress profiles is magnified. (b) shows the same profiles but for cases E, E1-E3; where the spacing s_x, s_y is changed.

decreases, by a relatively small amount. The ratio u_{*hi}/u_{*lo} is also of significance, and it is seen to increase with c_{ft}.

Next, we present the vertical profiles for the scalar flux. The total flux (q(z)) is given by the sum of the Reynolds, dispersive, and SGS fluxes, i.e. $q = \langle \overline{w'\theta'} \rangle + \langle \overline{w''\theta''} \rangle + \langle \bar{r}_3 \rangle$. At the surface, the flux is equal to the mean value of q_s arising from the boundary condition as in Eq. (6).

These are normalized with the geostrophic velocity U_G (obtained as before) and the scalar difference between the surface and the top of the domain, $(\theta_s - \theta_\infty)$. At the surface, overall an increase of the scalar flux of about $\sim 10\%$ can be observed for the cases with wind turbines as compared to the case without wind turbines. Figure 6(a) shows the profiles for cases A-G. A zoom-in from the lower region is presented on the top, right corner insert. There, a small increase in the scalar fluxes correlated with the increase in thrust coefficient can be observed. Similarly, Figure 6(b) shows the corresponding scalar flux profiles for cases E and E1-E3. Contrary to the momentum, the scalar flux increase occurs over the
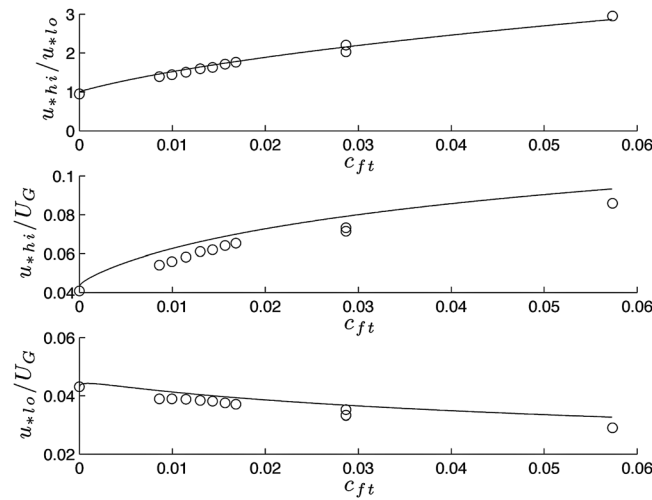
FIG. 5. Symbols: friction velocity ratios as function of loading coefficient. Lines: predictions of simple 1D model.[5] (a) Ratio u_{*hi}/u_{*lo} (see Eq. (23)); (b) u_{*hi}/U_G (see Eq. (7)) and (c) u_{*lo}/U_G (from (a) and (b)).

boundary layer at $z < 5z_h$, without any sudden signature from the wind turbines in the scalar flux profiles. This illustrates the significantly different behaviors exhibited by the scalar and momentum fluxes. Clearly the Reynolds analogy does not hold, essentially due to the fact that the wind turbines affect the momentum and kinetic energy (a direct effect) very differently than they affect scalar fluxes (only indirect effects).

To quantify the effects of the increase in the scalar fluxes on the scalar profiles, we obtain the horizontally averaged scalar difference profiles, $(\theta_s - \langle \bar{\theta} \rangle (z))/(\theta_s - \theta_\infty)$. These are presented in Figure 7(a) for cases A to G and Figure 7(b) for cases E and E1-E3. It is observed that in the presence of wind turbines, the scalar gradient close to the surface is accentuated. Induced by the increase of mixing, air with lower scalar concentration from the layer above the wind turbines is entrained downward. This induced change in the scalar vertical profiles is consistent with the increase in scalar fluxes.

Similar to Figure 5, we plot in Figure 8 the ratio of scalar flux measured from the LES at some reference height above the wind turbines, say, $z = 1.5z_h$ with and without wind turbines present, as function of loading parameter c_{ft}. This plot illustrates more clearly that the scalar fluxes increase by about 10%–15% and depend rather weakly on loading parameter.

In Sec. IV, we discuss these results in the context of a simple 1D (column) model of the WTABL including scalar transport.

IV. SINGLE COLUMN MODELING OF THE WTABL

A. Double log-layer mean velocity distribution including wake layer

In Calaf *et al.*,[5] a new model describing the surface roughness induced by a large wind farm was introduced. The model follows the approach of Frandsen[25] and Frandsen *et al.*[28] based on log-layer profiles, above and below the
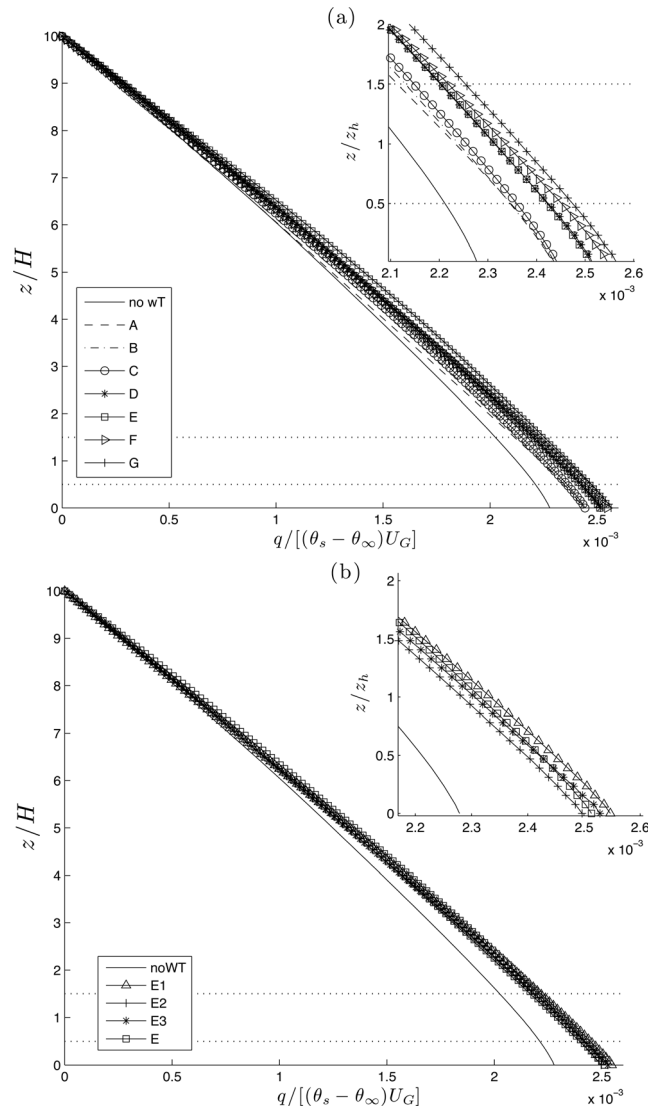

FIG. 6. Vertical profiles of the total passive scalar flux for wind farms with different loading coefficients. (a) shows the profiles for cases A to G, where only the thrust coefficient is changed. (b) shows the same profiles but for cases E and E1-E3, where the spacing s_x, s_y is changed. On the top, right corner insert in both plots, the lower 20% of the domain height is shown to examine the scalar flux profiles in more detail.

wind turbine region. To obtain more accurate results, the approach also includes a wind turbine wake region, where increased mixing leads to flatter mean velocity profiles.

Based on momentum balance for a fully developed ABL, Frandsen[25] and Frandsen *et al.*[28] derived an expression for the induced wind farm surface roughness length $z_{0,hi}$. They assumed the existence of two equilibrium logarithmic layers: one above the wind turbine array, characterized by an upper friction velocity (denoted as u_{*hi} with "high" denoted by subscript "*hi*," as in Calaf *et al.*[5]), and one below characterized by a second friction velocity u_{*lo} ("low" denoted by subscript "*lo*"). Both logarithmic mean velocity profiles were assumed to meet at hub-height. Moreover, the momentum balance was used to relate the difference between the two momentum fluxes to the momentum loss in the wake region, due to the thrust on the wind turbines, according to
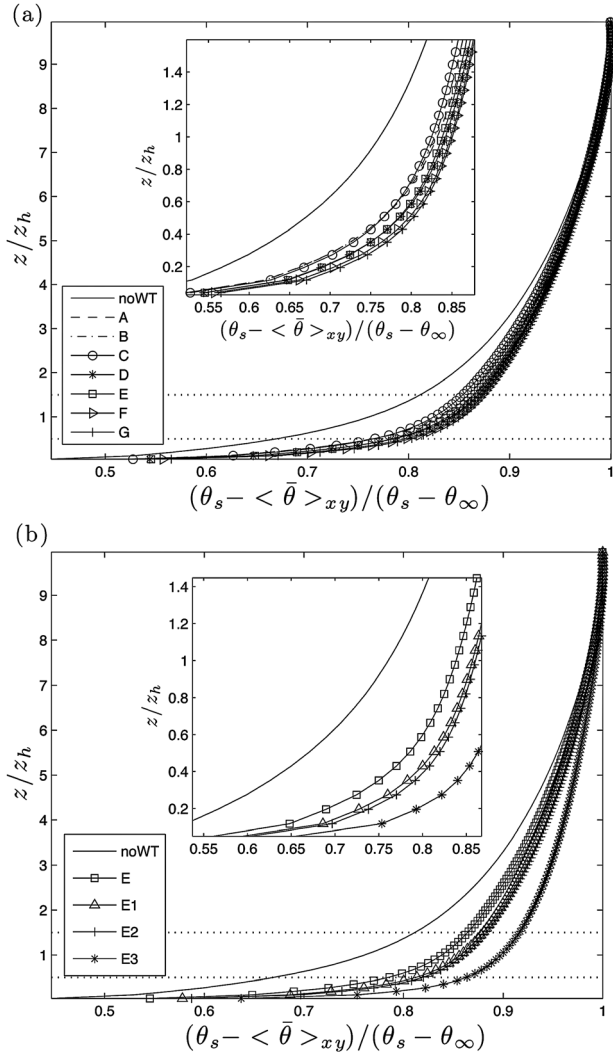
(a)

(b)

FIG. 7. Vertical profiles of the scalar difference between the surface and a given height $(\theta_s - \langle\bar{\theta}\rangle(z))$, normalized by the scalar difference between the surface and the top of the domain, $(\theta_s - \theta_\infty)$ for the different study scenarios. (a) shows the profiles for cases A to G, where only the thrust coefficient is changed. (b) shows the same profiles for cases E and E1-E3; where the spacing s_x, s_y is changed. The centered small inserts in both plots show the lower 15% of the domain height so it is possible to examine the profiles in more detail close to the ground.

$$u_{*lo}^2 = u_{*hi}^2 + \frac{1}{2} C_T \left(\frac{\pi}{4} D^2\right) [\langle\bar{u}\rangle(z_h)]^2 \left(\frac{1}{s_x s_y D^2}\right). \quad (16)$$

In this expression, C_T is the standard thrust coefficient, and the upstream velocity scale is taken to be the horizontal mean velocity at hub-height, $\langle\bar{u}\rangle(z_h)$. The expression can be further simplified to read

$$u_{*lo}^2 = u_{*hi}^2 + \frac{1}{2} c_{ft}[\langle\bar{u}\rangle(z_h)]^2, \quad (17)$$

where $c_{ft} = \pi C_T/(4 s_x s_y)$ as in Sec. III.

Generalizing the approach of Frandsen[25] and Frandsen et al.,[28] in Calaf et al.,[5] three layers are assumed to exist. As in Frandsen[25] and Frandsen et al.,[28] the first layer is a constant stress layer below the turbines, where the stress is u_{*lo}^2 and the eddy-viscosity is $\kappa z u_{*lo}$ (κ is the von Kármán constant),
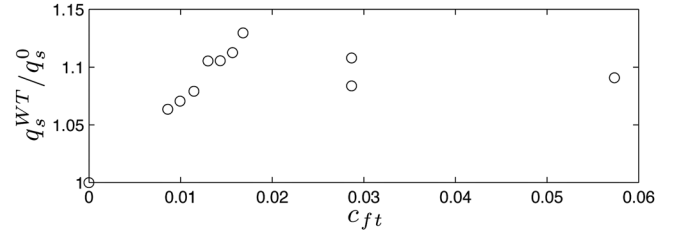

FIG. 8. Symbols: Ratio of scalar flux with and without wind turbines (evaluated at a height $1.5 z_h$), as function of wind farm loading parameter c_{ft}.

$$(\kappa z u_{*lo}) \frac{d\langle\bar{u}\rangle}{dz} = u_{*lo}^2 \Rightarrow \langle\bar{u}\rangle(z)$$
$$= \frac{u_{*lo}}{\kappa} \ln\left(\frac{z}{z_{0,lo}}\right), \quad \text{for} \quad z_{0,lo} < z < z_h - \frac{D}{2}. \quad (18)$$

In the wind turbine region, it is assumed that another layer exists,[5] where increased eddy-mixing is induced due to the wakes. In this wake layer, the eddy-viscosity is increased from its baseline boundary layer value $\kappa z u_*$ by an additional wake eddy-viscosity ν_w

$$(\kappa z u_* + \nu_w) \frac{d\langle\bar{u}\rangle}{dz} = u_*^2 \Rightarrow \left(1 + \nu_w^*\right) \frac{d\langle\bar{u}\rangle}{d\ln(z/z_h)}$$
$$= \frac{u_*}{\kappa}, \quad \text{for} \quad z_h - \frac{D}{2} < z < z_h + \frac{D}{2}, \quad (19)$$

where $\nu_w^* = \nu_w/(\kappa u_* z) \approx \sqrt{\frac{1}{2} c_{ft}} \langle\bar{u}(z_h)\rangle D/(\kappa u_* z_h) \approx 28\sqrt{\frac{1}{2} c_{ft}}$ (see Calaf et al.[5] for details), and the friction velocity is taken as $u_* = u_{*lo}$ for $z_h - D/2 < z < z_h$ and as $u_* = u_{*hi}$ for $z_h < z < z_h + D/2$. The third layer is another constant stress layer above the turbine region $z > z_h + D/2$, where the stress is u_{*hi}^2, the eddy-viscosity is $\kappa z u_{*hi}$, and the velocity offset is described by an effective wind farm roughness length $z_{0,hi}$,

$$(\kappa z u_{*hi}) \frac{d\langle\bar{u}\rangle}{dz} = u_{*hi}^2 \Rightarrow \langle\bar{u}\rangle(z)$$
$$= \frac{u_{*hi}}{\kappa} \ln\left(\frac{z}{z_{0,hi}}\right), \quad \text{for} \quad z > z_h + \frac{D}{2}. \quad (20)$$

Returning to the middle layer, integrating and matching mean velocities at $z = z_h - D/2$ and $z = z_h + D/2$ yields

$$\langle\bar{u}\rangle(z) = \frac{u_{*lo}}{\kappa} \ln\left[\left(\frac{z}{z_h}\right)^{\frac{1}{1+\nu_w^*}} \left(\frac{z_h}{z_{0,lo}}\right) \left(1 - \frac{D}{2 z_h}\right)^\beta\right], \quad \text{for}$$
$$z_h - \frac{D}{2} < z < z_h, \quad (21)$$

and

$$\langle\bar{u}\rangle(z) = \frac{u_{*hi}}{\kappa} \ln\left[\left(\frac{z}{z_h}\right)^{\frac{1}{1+\nu_w^*}} \left(\frac{z_h}{z_{0,hi}}\right) \left(1 + \frac{D}{2 z_h}\right)^\beta\right], \quad \text{for}$$
$$z_h < z < z_h + \frac{D}{2}, \quad (22)$$

where the exponent $\beta = \nu_w^*/(1+\nu_w^*)$ is introduced to simplify the notation.[5] Equality of these two expressions at $z=z_h$ enables us to derive the relationship between the two friction velocities in the form of

$$u_{*lo} = u_{*hi} \frac{\ln\left[\dfrac{z_h}{z_{0,hi}}\left(1+\dfrac{D}{2z_h}\right)^{\beta}\right]}{\ln\left[\dfrac{z_h}{z_{0,lo}}\left(1-\dfrac{D}{2z_h}\right)^{\beta}\right]}. \tag{23}$$

By substituting this relationship into the momentum balance (Eq. (17)) and replacing the mean velocity $\langle \bar{u}\rangle(z_h)$ with Eq. (22) evaluated at $z=z_h$, an equation for the effective roughness height is obtained, leading to the expression

$$z_{0,hi} = z_h\left(1+\frac{D}{2z_h}\right)^{\beta}$$
$$\times \exp\left(-\left[\frac{c_{ft}}{2\kappa^2}+\left(\ln\left[\frac{z_h}{z_{0,lo}}\left(1-\frac{D}{2z_h}\right)^{\beta}\right]\right)^{-2}\right]^{-1/2}\right). \tag{24}$$

For further details on the theoretical basis and mathematical development, see Calaf *et al.*[5] For a given geostrophic wind forcing velocity U_G, the knowledge of the effective roughness $z_{0,hi}$ enables the determination of the friction velocity u_{*hi} based on Eq. (7).

B. Scalar distribution in single column model of the WTABL

In this section, the derivation follows the same steps as Sec. IV A, but now for the mean passive scalar field $\bar{\theta}$ averaged in horizontal directions. The main difference is that unlike for momentum, the wind turbines do not directly add or extract scalar fluxes (i.e., we assume wind turbines do not themselves cool or heat the air or absorb scalar concentrations, etc.). Another difference is that the turbulence diffusivity in the wake region may involve different turbulent Prandtl numbers as in the background unperturbed boundary layer flow.

From Monin-Obukhov similarity theory and eddy-diffusion model, for an imposed scalar value at the surface of θ_s, the surface scalar flux q_s in the atmospheric surface layer is related with the shear stress (friction velocity) at the surface, and the scalar gradient according to

$$\frac{u_*\kappa z}{Pr_T}\frac{d[\theta_s - \langle\bar{\theta}\rangle(z)]}{dz} = q_s, \tag{25}$$

where u_* is the friction velocity and Pr_T is the turbulent Prandtl number. Equation (25) yields a logarithmic scalar difference profile and relates the scalar flux to scalar concentrations at various heights. Now we consider the case without wind-turbines as a reference case and denote the corresponding scalar flux and other variables with a superscript 0. In particular, if we assume that $\tilde{\theta}(H_G) = \theta_\infty$ at the boundary

layer height H_G, for which we take the classical value $H_G = exp(-\kappa C)\frac{u_*}{f}$, where $C=4$ and $f=2\Omega\sin\phi$ is (as before) the Coriolis parameter, we can express a relationship between the overall scalar difference between the surface and above the boundary layer and the scalar flux q_s^0 as follows:

$$\theta_s - \theta_\infty = \frac{Pr_T^0 q_s^0}{\kappa u_*}\left[\ln\left(\frac{u_*}{fz_{0,s}}\right) - \kappa C\right]. \tag{26}$$

Next, we consider the case with wind turbines, in which the eddy-diffusivities change according to which layer one is in, because the friction velocities change below and above the hub-height. In analogy with the momentum balance, we now assume that below the wind turbine area, the eddy diffusivity is given by $\kappa z u_{*lo}(Pr_T^{WT})^{-1}$ and thus

$$\left[(Pr_T^{WT})^{-1}\kappa z u_{*lo}\right]\frac{d\left(\theta_s - \langle\bar{\theta}\rangle\right)}{dz} = q_s^{WT} \Rightarrow \theta_s - \langle\bar{\theta}\rangle(z)$$
$$= Pr_T^{WT}\frac{q_s^{WT}}{\kappa u_{*lo}}\ln\left(\frac{z}{z_{0,s}}\right),$$
$$\text{for}\quad z_{0,s} < z < z_h - D/2. \tag{27}$$

In the wind turbine region, it is assumed again that increased eddy-mixing is induced due to the wakes. In this layer, the eddy-diffusivity is increased from its baseline boundary layer value by the wake eddy-diffusivity $(Pr_T^{WT})^{-1}\nu_w$. Therefore,

$$(Pr_T^{WT})^{-1}(\kappa z u_* + \nu_w)\frac{d\left(\theta_s - \langle\bar{\theta}\rangle\right)}{dz}$$
$$= q_s^{WT} \Rightarrow \left(1+\nu_w^*\right)\frac{d\left(\theta_s - \langle\bar{\theta}\rangle\right)}{d\ln(z/z_h)}$$
$$= Pr_T^{WT}\frac{q_s^{WT}}{u_*\kappa}, \quad \text{for}\quad z_h - D/2 < z < z_h + D/2, \tag{28}$$

where as before, $\nu_w^* = \nu_w/(\kappa u_* z) \approx \sqrt{\frac{1}{2}c_{ft}}\langle\bar{u}(z_h)\rangle D/(\kappa u_* z_h)$ $\approx 28\sqrt{\frac{1}{2}c_{ft}}$. Again, the friction velocity is taken as $u_* = u_{*lo}$ for $z_h - D/2 < z < z_h$ and as $u_* = u_{*hi}$ for $z_h < z < z_h + D/2$. In the layer above the turbine region, $z > z_h + D/2$, there is no additional eddy-diffusivity due to wakes, but the relevant friction velocity is now u_{*hi}. Then

$$\left[(Pr_T^{WT})^{-1}\kappa z u_{*hi}\right]\frac{d\left(\theta_s - \langle\bar{\theta}\rangle\right)}{dz}$$
$$= q_s^{WT} \Rightarrow \theta_s - \langle\bar{\theta}\rangle(z)$$
$$= Pr_T^{WT}\frac{q_s^{WT}}{\kappa u_{*hi}}\ln(z) + A, \quad \text{for}\quad z > z_h + D/2, \tag{29}$$

and the constant of integration A is selected so that at the boundary layer height H_G^{WT}, the scalar equals the imposed scalar above the boundary layer, namely $\langle\bar{\theta}\rangle(H_G^{WT}) = \theta_\infty$. Then, Eq. (28) can be integrated between $z_h - D/2$ and z_h using $u_* = u_{*lo}$, and between z_h and $z_h + D/2$ using $u_* = u_{*hi}$. Matching the solution with that of Eq. (29) at

$z = z_h + D/2$ leads to a relationship between the overall scalar difference and the scalar flux as follows:

$$\theta_s - \theta_\infty = \frac{Pr_T^{WT} q_s^{WT}}{\kappa u_{*hi}} \left[\ln\left(\frac{H_G}{z_h} \left(1 + \frac{D}{2z_h} \right)^{-\beta} \right) \right.$$
$$\left. + \frac{u_{*hi}}{u_{*lo}} \ln\left(\frac{z_h}{z_{0,s}} \left(1 - \frac{D}{2z_h} \right)^{\beta} \right) \right]. \qquad (30)$$

In the integration process and as a first approximation, the parameter Pr_T^{WT} is considered constant with height. In the absence of wind turbines, we assume that the "unperturbed" friction velocity is u_*.

Solving for the scalar flux with wind turbines and replacing H_G in terms of the geostrophic quantities, $H_G^{WT} = \exp(-\kappa C)(u_{*hi}/f)$, its ratio with the scalar flux without wind turbine becomes

$$\frac{q_s^{WT}}{q_s^0} = \frac{u_{*hi}}{u_*} \frac{Pr_T^0}{Pr_T^{WT}} \left\{ \frac{\ln\left(\frac{u_{*hi}}{fz_{0,s}} \right) - \kappa C + \frac{u_{*hi}}{u_{*lo}} \ln\left[\frac{z_h}{z_{0,s}} \left(1 - \frac{D}{2z_h} \right)^{\beta} \right] - \ln\left[\frac{z_h}{z_{0,s}} \left(1 + \frac{D}{2z_h} \right)^{\beta} \right]}{\ln\left(\frac{u_*}{fz_{0,s}} \right) - \kappa C} \right\}. \qquad (31)$$

Finally, everything is expressed in terms of the geostrophic wind velocity since this is the common driving force that sets the turbulence levels (friction velocities) u_* and u_{*hi} and u_{*lo} in all cases. For this purpose, we use the approximation described in the Appendix of Calaf *et al.*[5] (for a discussion of its accuracy, about 7%, see discussion in Meyers and Meneveau[39])

$$u_* = \frac{\kappa U_G}{\ln\left(\frac{U_G}{fz_0} \right) - C_*}, \qquad (32)$$

with $C_* = 4.5$. Using this expression with $z_0 = z_{0,lo}$ gives the unperturbed value of the friction velocity without wind turbines, u_*. Using it with $z_0 = z_{0,hi}$ (determined using Eq. (24)) gives u_{*hi}. As a result, the first ratio in Eq. (31) is

$$\frac{u_{*hi}}{u_*} = \left[1 - \frac{\ln\left(\frac{z_{0,hi}}{z_{0,lo}} \right)}{\ln\left(\frac{U_G}{fz_{0,lo}} \right) - C_*} \right]^{-1}. \qquad (33)$$

The last equation needed is the ratio of the two friction velocities u_{*hi}/u_{*lo} which is obtained from Eq. (23), where $z_{0,hi}$ is determined as before using Eq. (24). The Prandtl number ratio is also an important variable for which we do not have an analytical expression. The relevance of this term and its value is discussed in Sec. V.

V. DISCUSSION: COMPARING LES WITH 1D WTABL MODEL

In this section, the ratios of scalar and momentum fluxes with and without wind turbines that were presented in Sec. IV B through Eqs. (31) and (33) are compared to the values obtained from the LES. Initial comparisons in which it was assumed that the ratio of Prandtl numbers is unity (i.e., $Pr_T^0 = Pr_T^{WT}$) showed significant differences between model predictions and LES results. It was found that the reason for discrepancies could be traced directly to the behavior of the Prandtl number, which was found to differ significantly for the case with and without wind turbines.

The LES Prandtl number is obtained by computing the ratio of the total eddy-viscosity with the total eddy-diffusivity. The first one results of dividing the total shear stress by the mean stream-wise velocity gradient, and the second one is computed by dividing the total scalar flux by the scalar gradient, namely

$$Pr_T = \frac{(\langle \tau_{xz} \rangle / \partial_z \langle \overline{u} \rangle)}{-(\langle q_s \rangle / \partial_z \langle \overline{\theta} \rangle)}. \qquad (34)$$

The results are shown in Figure 9. As is shown in Figure 9(a) (case E, as a representative example), the vertical profile of the ratio shows vertical variations especially in the wind turbine region. However, in developing the theoretical model, it was useful to assume a constant value. Figure 9(b) shows the Prandtl number ratio Pr_T^0/Pr_T^{WT} as a function of c_{ft} for three different heights. The hollow squares in Figure 9(b) are the LES results for the ratio of the Prandtl numbers at $z/z_h = 1.5$. The dotted-dashed line represents an exponential fit to these values. Similarly, the hollow circles and the triangles represent the LES results at $z/z_h = 2$ and $z/z_h = 3$. As can be seen, the ratio tends to unity for diminishing wind-turbine loading conditions ($c_{ft} \to 0$), but the results asymptote to different values at large loading depending on the height. From the vertical profiles (e.g., Figure 9(a)), it is apparent that the region over which the Prandtl number is mostly constant is above the wind turbine region, at a height around $z = 2z_h$. Therefore, we use this height in choosing a representative ratio of Prandtl numbers.

The results from the LES are approximated by fitting exponential functions. The chosen exponential function is given by

$$\left. \frac{Pr_T^0}{Pr_T^{WT}} \right|_{z/z_h = 2} = ae^{bc_{ft}} + ce^{dc_{ft}}, \qquad (35)$$

with $a = 1.13$, $b = 1.96$, $c = -0.13$, and $d = -148$, for $z/z_h = 2$. The thick solid line in Figure 9(b) shows the fit. Dashed and dotted-dashed lines show fits at the other two heights, although these are not used. At $c_{ft} = 0$, the fit yields unit ratio, as required for the case without wind turbines.
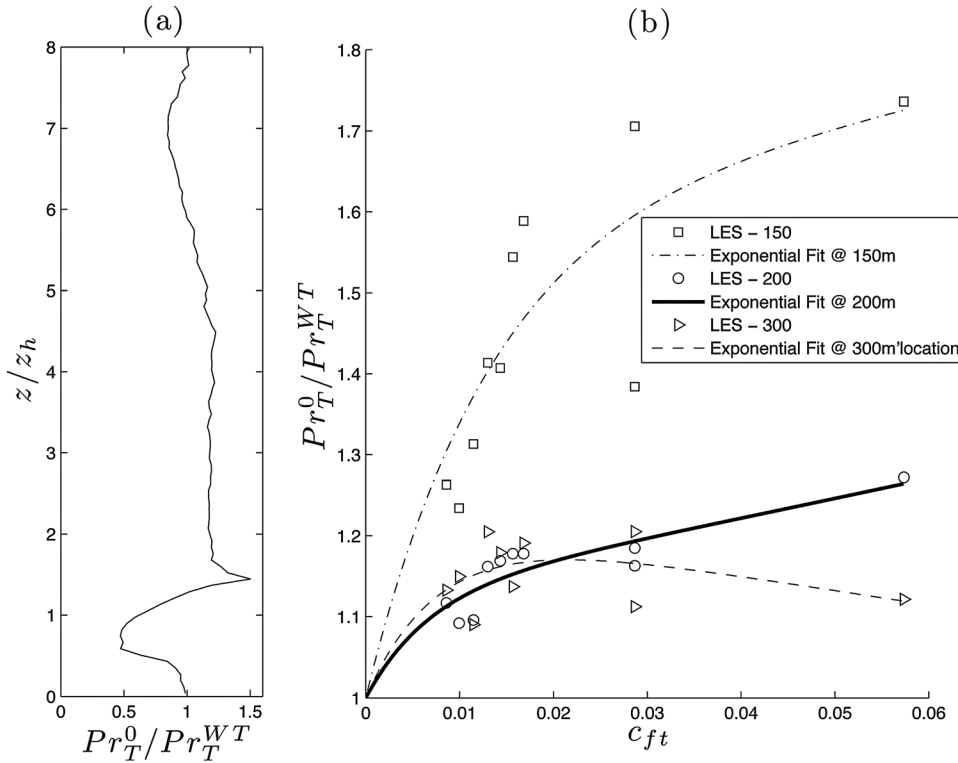
FIG. 9. Prandtl number ratio Pr_T^0/Pr_T^{WT} obtained from LES and empirical fits. (a) shows a sample vertical profile of the ratio of Prandtl numbers from LES case E, with $c_{ft} = 0.0143$. (b) shows the ratio as a function of c_{ft} for three different heights above the wind turbine region. The hollow squares are the LES values at $z/z_h = 1.5$. The dotted-dashed line represents an exponential fit to these values. Similarly, the hollow circles and the triangles represent the LES values at $z/z_h = 2$ and $z/z_h = 3$, respectively. The thick solid line and the dashed line are their corresponding exponential fits used in the model.

Having used the LES to parameterize the ratio of Prandtl numbers, the model predictions for the ratio of scalar fluxes can now be examined. Figure 10 shows (middle curves) the ratio of scalar fluxes predicted from the model (Eq. (31), dark solid line) and LES results (hollow triangles), as a function of c_{ft}. The model shows that this ratio increases with increasing c_{ft} up to a certain point, from which this ratio slightly decreases. Nevertheless, the ratio is always above 1, meaning that when there are wind turbines present, the scalar flux is increased no matter what is the loading of the wind farm. However, the increase is not large, smaller than 20%, typically around 15%. The LES results also showed an increase in the scalar flux ratio with increasing c_{ft} up to a certain point and later decreases in qualitative agreement with the trends of the model. However, details of the two curves differ. For instance, the peak ratio occurs near $c_{ft} \approx 0.01$ for the model, whereas it seems to occur close to $c_{ft} \approx 0.018$ from the LES.

To asses the origin of these quantitative differences, each dominant term that occurs in Eq. (31) is analyzed separately. The first term of interest is the ratio u_{*hi}/u_* in Eq. (31). It describes the increase of scalar flux due to the fact that the friction velocity above wind turbines will be increased as compared to the case without wind turbines, when the same geostrophic wind velocity U_G forces the flow. The model's prediction for this term (Eq. (33)) is shown as dotted-dashed line. The circles show the ratio as determined from the LES, in which the friction velocity u_{*hi} was already determined in Sec. III in terms of the total stress at height $z_h + D/2$. The agreement between model and simulation results is quite good over the entire range, in terms of overall trends, although the model over-predicts the ratio slightly. The largest discrepancies occur for the first three points at low c_{ft}.

The remaining factor, containing the ratio of Prandtl numbers and the last term in Eq. (31), is also plotted. The dashed line shows the model expression. The hollow squares display the LES results. These are obtained simply by taking the measured scalar flux ratio and dividing by the ratio (u_{*hi}/u_*) of measured friction velocities. The last factor in Eq. (31) is monotonically decreasing as the loading increases (increasing c_{ft}). This term represents the effects of the decreased momentum transport below the wind turbine
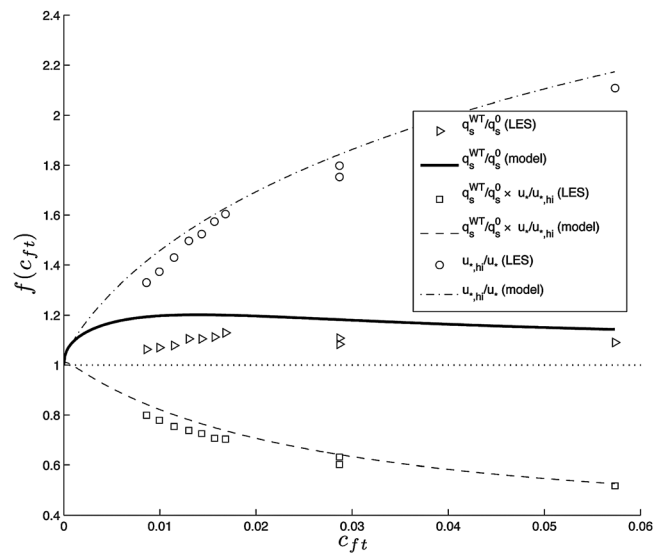

FIG. 10. Solid line: ratio of scalar fluxes obtained using Eq. (31), as a function of c_{ft}. Hollow triangles: ratio of scalar fluxes obtained from LES data. The ratio u_{*hi}/u_* (first factor in right-hand-side of Eq. (31)) is plotted in the same figure with dotted-dashed line, while the open circles show the LES values. Finally, the remaining factors on the right-hand-side of Eq. (31) are also plotted (dashed line for the model, and open squares for the LES results).

region. As can be seen, the model captures the overall LES trends quite well, with some underestimation of the ratio.

We can conclude that the model for the scalar flux in the presence of wind turbines predicts quite accurately the relatively small increase in the scalar flux observed in the LES results. However, the observed differences in the predicted ratio of scalar fluxes can be attributed mainly to the relatively small differences of model and LES values of the factor u_{*hi}/u_* for the first values (low $c_{\rm ft}$ cases). This is further discussed in Sec. VI.

It is worth mentioning that when comparing the 1D-model against the LES results, having to fit the Prandtl number ratio is less than ideal, but up to date we were not successful at deriving the Prandtl number ratio from any theory. For this reason, the 1D model is also compared against the LES data when removing the effect of the Prandtl number ratio fit in Figure 11. Figure 11(a) shows again the ratio of scalar fluxes. Now the vertical scale has a smaller range and, therefore, the differences between the analytical solution and the LES data are accentuated. Over the majority of the range, the difference is less than 10%, being close to ($\sim$13%) for the less loaded cases. Both the model and the LES data show an initial increase in the ratio of scalar fluxes with increasing $c_{\rm ft}$, then a slight decrease with loading. Figure 11(b) shows the same results but divided by the Prandtl number ratio in order to eliminate uncertainties associated with the empirical fit described above. As can be seen, without the effects of Prandtl numbers, the model and LES values show slightly improved agreement. Dividing this result now by the ratio u_{*hi}/u_*, the remaining expression represents purely the decreasing effects due to the wind turbine screening of momentum transport closest to the surface. As seen in Figure

11(c), the agreement between the model and LES results is excellent. Defining as usual the friction scalar value according to $\theta_* = q_s/u_*$, we conclude that the ratio $(\theta_*^{WT} Pr_T^{WT})/(\theta_* Pr_T^0)$ is very well predicted by the model. The main sources of error in Eq. (31) are the ratios u_{*hi}/u_* and Pr_T^0/Pr_T^{WT}; the first one being the most important.

Also of interest is to discuss the accuracy of the model in predicting the values of u_{*hi} and u_{*lo}. Figure 5(c) shows the behavior of u_{*lo} with increasing $c_{\rm ft}$. Friction velocities are now normalized by the driving velocity scale U_G for meaningful comparison. Initially, for very small $c_{\rm ft}$ coefficients, u_{*lo} remains almost constant without much noticing the effects of the wind turbines. Then for $c_{\rm ft} \sim 0.002$ and above, the wind turbines' effect is noticed leading to a decrease in u_{*lo} reaching a maximum decrease of about 33% for $c_{\rm ft} = 0.057$, compared with the friction velocity u_*/U_G without wind turbines (obtained from using the roughness length of the underlying surface, $z_{0,lo}$). For the friction velocity above the wind turbines, Figure 5(b) shows an increasing trend of u_{*hi} with increasing $c_{\rm ft}$, where u_{*hi} increases by almost $\sim$200% compared to the unloaded case without wind turbines. Note that this implies an increase of a factor of two for expected turbulence levels in the regions directly above the wind turbine area for highly loaded wind farms.

VI. CONCLUSIONS

The present simulation study has focused on the "fully developed wind turbine-array boundary layer." This concept was recently studied in detail by Calaf *et al.*[5] and now has been used to study the influence of large arrays of wind turbines on scalar transport. A suite of large eddy simulations in which wind turbines are modeled using the classic "drag disk" concept has been performed in order to quantify the scalar fluxes across the boundary layer and the influence that different wind farm loadings can have on it. The focus of the present paper is on horizontally averaged statistics. The LES results show an increase of the scalar flux of approximately 10%–15% and only a relatively small dependence upon loading. It was observed that the ratio of scalar fluxes increases for small $c_{\rm ft}$ values, but then the ratio slowly decreases with increasing loading. These trends are the result of two much larger trends that mostly cancel each other out: an increase of the friction velocity above the wind turbines and a decrease of friction velocity below the wind turbines.

Simulations have also been compared with a new "single column model" (1D) of the wind farm. The model is based on the description of the boundary layer including two logarithmic layers separated by a third layer, where additional mixing from the wind turbine wakes generates more blunt mean profiles, as introduced by Calaf *et al.*[5] There is overall reasonable agreement between the 1D model and the LES data, especially in terms of trends. In particular, there is excellent agreement between the LES data and the ratio $(\theta_*^{WT} Pr_T^{WT})/(\theta_* Pr_T^0)$, once the effects of Prandtl number are not included. The non-monotonic behavior of ratio of scalar fluxes is well described by the 1D model. The model confirms that there is a competition between increasing u_{*hi} and decreasing u_{*lo}. The second trend acts as an increased
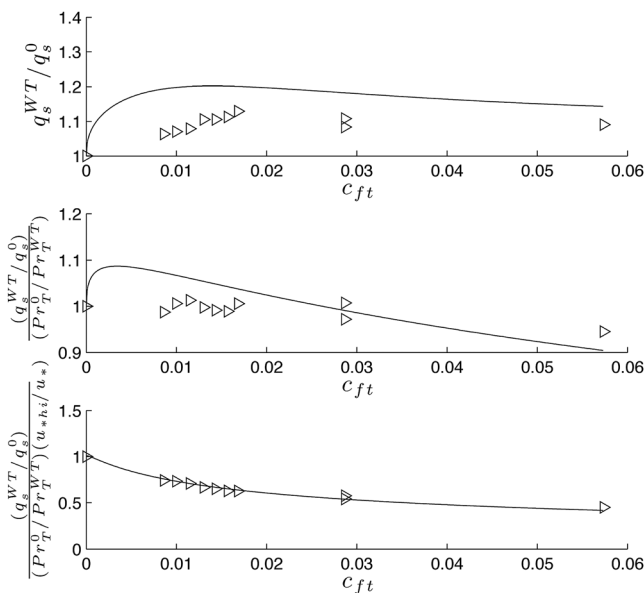
FIG. 11. Further detailed analysis of scalar flux ratios with and without wind turbines and comparison between single column model and LES results. The analytical results are presented as solid lines while LES results are shown as triangles. (a) shows the ratio of scalar fluxes; (b) shows the ratio of scalar fluxes divided by the ratio of Prandtl numbers; and (c) shows the ratio of scalar fluxes divided by the ratio of Prandtl numbers and also divided by the ratio u_{*hi}/u_* (corresponding to the last term in the right hand side of Eq. (31)).

resistance, reducing the amount of scalar flux extracted from the ground, when the loading grows. Still, the increasing u_{*hi} dominates slightly, thus increasing the overall scalar flux by about 10%–20%.

The results of this study were obtained using LES with a "drag disk" model for reproducing the effects of wind turbines. More detailed modeling, including moving blades, etc., would be more accurate, but then covering the entire boundary layer with multiple wind turbines would not be practical, especially when wishing to compute a suite of different cases with varying parameters. Overall, we believe that the "drag disk" approach captures the main aspects of the wind-turbine boundary layer interactions at the scales of interest in this study. Another approximation used in this study is the pressure-gradient forcing, coupling the results with classic relationships for relating surface layer scales with the geostrophic range, following the discussion presented in the Appendix of Calaf et al.[5] The underlying assumption of "separation of scales" is used in which it is assumed that the "inner region" at scales comparable to z_h and $z_{0,hi}$ is not directly affected by Coriolis accelerations. This is not exactly valid as one may expect some effects from Ekman-layer "flow turning," etc. Finally, the current simulations and models do not include stratification effects. A systematic study of stratification effects on the WTABL, and how to appropriately include such effects in 1D column models, is left as a future task.

We remark that very recently, a new LES study by Lu and Porté-Agel[41] provides valuable insights into various combined effects, including high-resolution of the near-turbine flow features using actuator line model, and including Coriolis and stratification effects. Their results also show increased vertical mixing of heat induced by the wind turbine motions, but with the atmospheric stratification providing additional effects on heat transport.

ACKNOWLEDGMENTS

APPENDIX: LAGRANGIAN SCALE-DEPENDENT SUBGRID MODEL FOR SCALARS

In most LES with potential temperature as a scalar variable, the subgrid Prandtl number is chosen to be a fixed constant value between 0.6 and 0.75. Porté-Agel[42] and Stoll and Porté-Agel[43] introduced a scale-dependent dynamic SGS model for scalars with averaging over horizontal surfaces.[42] This model was further improved with a Lagrangian averag-

ing[43] and shown to be a valuable tool when heterogeneous conditions are present.[44] The approach of Stoll and Porté-Agel[43] involved solving a high-order polynomial for the scale-dependence factor. Here, we combine the approach of Stoll and Porté-Agel[43] with the more approximate approach of Bou-Zeid et al.,[29] since the latter does not require solving polynomial equations at each point of the domain. The SGS scalar flux r_i is modeled using an eddy-diffusivity approach

$$r_i = -\frac{\nu_{SGS}}{Pr_{sgs}}\partial_i\tilde{\theta} = -\frac{C_{s,\Delta}^2\Delta^2|\tilde{S}|}{Pr_{sgs}}\partial_i\tilde{\theta} = -D_{s,\Delta}^2\Delta^2|\tilde{S}|\partial_i\tilde{\theta}, \quad \text{(A1)}$$

where Δ is the filtering length scale, and $|\tilde{S}| = \sqrt{2\tilde{S}_{ij}\tilde{S}_{ij}}$, with $\tilde{S}_{ij} = \frac{1}{2}(\partial_j\tilde{u}_i + \partial_i\tilde{u}_j)$. The SGS eddy-diffusivity coefficient $D_{s,\Delta}$ is obtained using a scale-dependent dynamic approach with a Lagrangian averaging approach similar to the one described in Bou-Zeid et al.[29] Following Moin et al.,[45] the Germano identity[46] is written for the scalar field as:

$$K_i \equiv \widehat{\tilde{u}_i\tilde{\theta}} - \widehat{\tilde{u}}_i\widehat{\tilde{\theta}} = R_i - \widehat{r_i}, \quad \text{(A2)}$$

where r_i is the SGS scalar flux at scale Δ, and R_i is the SGS scalar flux at scale $\alpha\Delta$ (with $\alpha = 2$). K_i is the resolved scalar flux, which can be computed from the resolved velocity and scalar fields through Eq. (A2). By assuming that $D_{s,\Delta}$ does not fluctuate too much in space, it can be extracted from the test-filtering operation, and $\widehat{r_i}$, R_i can be written as follows:

$$\widehat{r_i} = -D_{s,\Delta}\Delta^2\widehat{|\tilde{S}|\partial_i\tilde{\theta}}, \quad \text{(A3)}$$

$$R_i = -D_{s,2\Delta}(2\Delta)^2|\widehat{\tilde{S}}|\partial_i\widehat{\tilde{\theta}}. \quad \text{(A4)}$$

The error in the above model, when replacing these terms into Eq. (A2), is given by

$$e_i = K_i - (R_i - \widehat{r_i}) = K_i - D_{s,\Delta}^2 X_i, \quad \text{(A5)}$$

with

$$X_i = \Delta^2\left[\widehat{|\tilde{S}|\partial_i\tilde{\theta}} - 4\beta|\widehat{\tilde{S}}|\partial_i\widehat{\tilde{\theta}}\right] \quad \text{(A6)}$$

for $\alpha = 2$, and where $\beta_s = (D_{s,2\Delta}/D_{s,\Delta})$ is a parameter that accounts for possible scale dependency of $D_{s,\Delta}$. To obtain $D_{s,\Delta}$, we find the minimum of the square of the error (e_ie_i). Determining this term in a local way results in a highly variable coefficient that becomes numerically unstable. Therefore, some form of averaging is needed, in the same way as is done for the momentum SGS. Thus, the Lagrangian averaging technique has been adopted here, where the terms are averaged over time following fluid pathlines. Assuming scale-invariance ($\beta_s = 1$), one gets $D_{s,\Delta}^2$ as follows:

$$D_{s,\Delta}^2 = \frac{I_{KX}}{I_{XX}}, \quad \text{(A7)}$$

with

$$I_{KX} = \int_{-\infty}^t K_i X_i[\mathbf{z}(t'), t']W(t - t')dt' \quad \text{(A8)}$$

and

$$I_{XX} = \int_{-\infty}^{t} X_i X_i[\mathbf{z}(t'), t'] W(t - t') dt'. \tag{A9}$$

Above $\mathbf{z}(t')$ represents the previous positions of the fluid elements, and $W(\tau)$ is an exponential relaxation function, the same as used for the momentum subgrid model in Bou-Zeid et al.[29] As a result of this type of time-weighting, one obtains simple relaxation transport equations for I_{KX} and I_{XX}, which after numerical discretization (using low-order but fast first-order methods) can be written conveniently as

$$I_{KX}^{n+1}(\mathbf{x}) = H\{\epsilon[K_i X_i]^{n+1}(\mathbf{x}) + (1 - \epsilon)I_{KX}^n(\mathbf{x} - \widetilde{\mathbf{u}}^n \Delta t)\}, \tag{A10}$$

$$I_{XX}^{n+1}(\mathbf{x}) = \epsilon[X_i X_i]^{n+1}(\mathbf{x}) + (1 - \epsilon)I_{XX}^n(\mathbf{x} - \widetilde{\mathbf{u}}^n \Delta t), \tag{A11}$$

where ϵ is given by

$$\epsilon = \frac{\Delta t / T^n}{1 + \Delta t / T^n}, \quad T^n = 1.5\Delta(I_{KX}^n I_{XX}^n) \tag{A12}$$

and

$$H\{x\} = \left\{ \begin{array}{ll} x & \text{if } x \geq 0 \\ 10^{-32} & \text{otherwise} \end{array} \right\}.$$

We are interested in cases where a scale-dependent model is needed also for the scalar, where the previously made assumption $\beta_s = 1$ is no longer valid. For this, filtering over a secondary larger scale ($\alpha = 4$) is needed. Similar to the momentum case, the coefficient $D_{s,\Delta}$ is therefore finally obtained by

$$D_{s,\Delta}^2 = \frac{D_{s,2\Delta}^2}{D_{s,4\Delta}^2 / D_{s,2\Delta}^2} = \frac{I_{KX}/I_{XX}}{max\{(I_{PY}I_{XX})/(I_{YY}I_{KX}), 0.125\}}, \tag{A13}$$
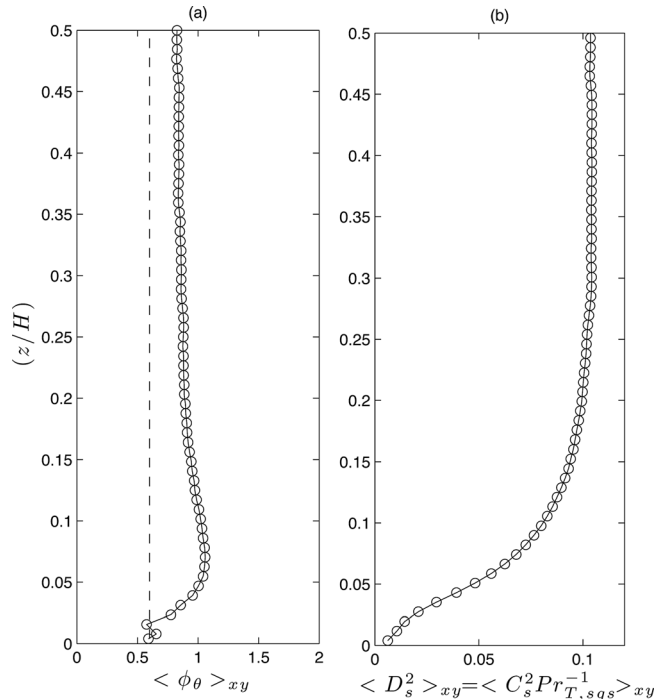
with $P_i = \overline{\widetilde{u}_i \widetilde{\theta}} - \overline{\widetilde{u}}_i \overline{\widetilde{\theta}}$, and $Y_i = \Delta^2 \left[\overline{|\widetilde{S}|\partial_i \widetilde{\theta}} - 16\beta \overline{|\widetilde{S}|}\overline{\partial_i \widetilde{\theta}} \right]$. The solid overline indicates filtering at scale 4Δ. The Lagrangian time average of the product of these terms is given by

$$I_{PY} = \int_{-\infty}^{t} P_i Y_i[\mathbf{z}(t'), t'] W(t - t') dt' \tag{A14}$$

and

$$I_{YY} = \int_{-\infty}^{t} Y_i Y_i[\mathbf{z}(t'), t'] W(t - t') dt', \tag{A15}$$

which in turn is numerically discretized, similar to what was done before

$$I_{PY}^{n+1}(\mathbf{x}) = H\{\epsilon[P_i Y_i]^{n+1}(\mathbf{x}) + (1 - \epsilon)I_{PY}^n(\mathbf{x} - \widetilde{\mathbf{u}}^n \Delta t)\}, \tag{A16}$$

$$I_{YY}^{n+1}(\mathbf{x}) = \epsilon[Y_i Y_i]^{n+1}(\mathbf{x}) + (1 - \epsilon)I_{YY}^n(\mathbf{x} - \widetilde{\mathbf{u}}^n \Delta t). \tag{A17}$$

The Lagrangian scale dependent sub-grid model for scalars is an adaptation of the original Lagrangian scale dependent sub-grid model of Bou-Zeid et al.[29] to better account for the spatial and temporal variability of scalars. For further details on the conceptual basis of the technique, see Bou-Zeid et al.[29]
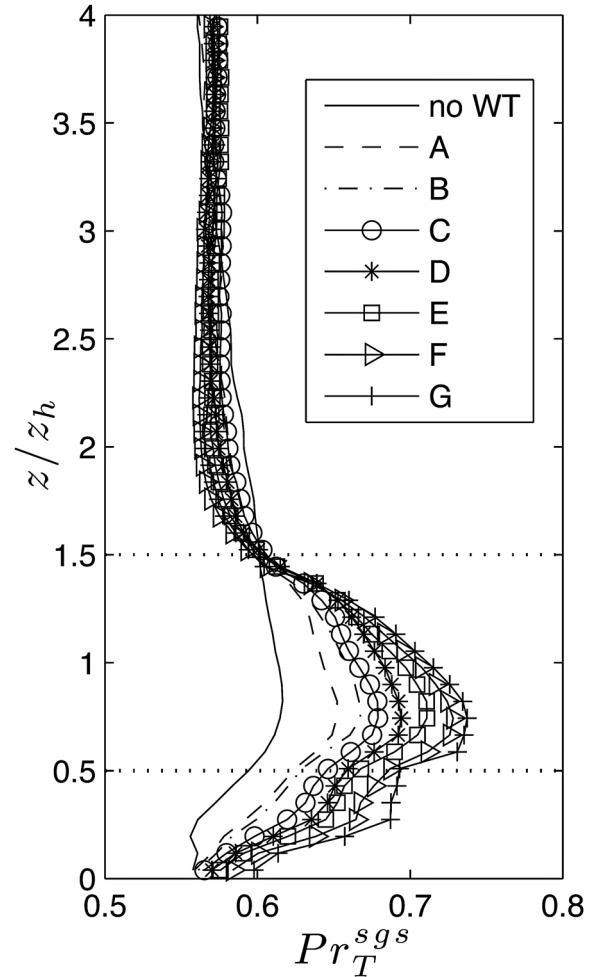

FIG. 13. Vertical profile of the subgrid turbulent Prandtl number. The solid line shows the case with no wind turbines. The dashed line shows the less loaded wind farm scenario (A; $C_T^t = 0.6$), with increasing thrust coefficient and the further the lines are shifted towards the right.

FIG. 12. Vertical profiles of the ϕ_θ function (a) and the scalar sub-grid coefficient (b).

Figure 12(a) shows a vertical profile of the φ_θ function for the case where there is no wind turbines, and Figure 12(b) shows the scalar sub-grid coefficient. Both show the expected behavior. Figure 13 shows the relevance of using a fully dynamic SGS model for the scalar fluxes. A vertical profile of the subgrid Prandtl number is presented for various cases simulated. This is obtained by dividing the horizontal averages of the momentum and scalar sub-grid coefficients: $Pr_T^{sgs} = \langle C_{s,\Delta}^2 \rangle / \langle D_{s,\Delta}^2 \rangle$ (here $C_{s,\Delta}^2$ represents the momentum sub-grid scale coefficient, where the sub-grid stress tensor is given by $\tau_{ij} = -2C_{s,\Delta}^2 \Delta^2 |\tilde{S}| \tilde{S}_{ij}$). As is apparent, the Prandtl number is not constant, especially close to the ground and in the wind turbine wake region. The solid line shows the case with no wind turbines for which the dynamically obtained SGS Prandtl number is between 0.55 and 0.6, i.e., similar to the normally assumed values. For the case with wind turbines, even the less loaded wind farm scenario (dashed line for the case with $C_T' = 0.6$), there is a noticeable effect due to wind turbines, with an increase in SGS Prandtl number. It implies that the SGS range of scales provide a larger increase in momentum mixing compared to scalar mixing. The increase of momentum mixing (more than scalar) in the wake of the wind turbines has a direct influence on Pr_T^{SGS}. This effect increases in magnitude as a function of the thrust coefficient.

[1] S. Baidya-Roy, S. W. Pacala, and R. L. Walko, "Can large scale wind farms affect local meteorology?," J. Geophys. Res. **109**, D19101, doi:10.1029/2004JD004763 (2004).

[2] S. Baidya-Roy and J. Justin Traiteur, "Impacts of wind farms on surface air temperatures," Proc. Natl. Acad. Sci. U.S.A. **107**, 17899 (2010).

[3] D. Keith, J. DeCarolis, D. Denkenberger, D. Lenschow, S. Malyshev, S. Pacala, and P. J. Rasch, "The influence of large-scale wind power on global climate," Proc. Natl. Acad. Sci. U.S.A. **101**, 16115 (2004).

[4] D. Barrie and D. Kirk-Davidoff, "Weather response to management of large wind turbine array," Atmos. Chem. Phys. **10**, 769 (2010).

[5] M. Calaf, C. Meneveau, and J. Meyers, "Large eddy simulation study of fully developed wind-turbine array boundary layers," Phys. Fluids **22**, 015110 (2010).

[6] R. B. Cal, J. Lebrón, H. S. Kang, L. Castillo, and C. Meneveau, "Experimental study of the horizontally averaged flow structure in a model wind-turbine array boundary layer," J. Renewable Sustainable Energy **2**, 013106 (2010).

[7] H. Snel, "Review of the present status of rotor aerodynamics," Wind Energy **1**(S1), 46 (1998).

[8] T. Burton, D. Sharpe, N. Jenkins, and E. Bossanyi, *Wind Energy Handbook* (John Wiley & Sons, Ltd., Hoboken, New Jersey, 2001).

[9] A. Crespo and J. Hernández, "Turbulence characteristics in wind-turbine wakes," J. Wind Eng. Ind. Aerodyn. **61**, 71 (1996).

[10] J. Whale, C. G. Anderson, R. Bareiss, and S. Wagner, "An experimental and numerical study of the vortex structure in the wake of a wind turbine," J. Wind Eng. Ind. Aerodyn. **84**, 1 (2000).

[11] L. A. Ivanova and E. D. Nadyozhina, "Wind flow deformation inside the wind farm," J. Wind Eng. Ind. Aerodyn. **74–76**, 389 (1998).

[12] P. R. Ebert and D. H. Wood, "The near wake of a model horizontal-axis wind turbine—II. General features of the three-dimensional flow field," Renewable Energy **18**, 513 (1999).

[13] M. Magnusson and A.-S. Smedman, "Air flow behind wind turbine," J. Wind Eng. Ind. Aerodyn. **80**, 169 (1999).

[14] L. J. Vermeer, J. N. Sorensen, and A. Crespo, "Wind turbine wake aerodynamics," Prog. Aerosp. Sci. **39**, 467 (2003).

[15] J. N. Sorensen and W. Z. Shen, "Numerical modeling of wind turbine wakes," J. Fluids Eng. **124**, 393 (2002).

[16] D. Medici and P. H. Alfredsson, "Measurements on a wind turbine wake: 3D effects and bluff body vortex shedding," Wind Energy **9**, 219 (2006).

[17] L. P. Chamorro and F. Porté-Agel, "A wind-tunnel investigation of wind-turbine wakes: Boundary-layer turbulence effects," Boundary-Layer Meteorol. **132**, 1299 (2009).

[18] P. R. Ebert and D. H. Wood, "The near wake of a model horizontal-axis wind turbine—I. Experimental arrangements and initial results," Renewable Energy **12**, 225 (1997).

[19] U. Hogstrom, D. N. Asimakopoulos, H. Kambezidis, C. G. Helmis, and A. Smedman, "A field study of the wake behind a 2 MW wind turbine," Atmos. Environ. **22**, 803 (1988).

[20] J. Kline, "Turbulence characteristics at Howden wind park I," in AWEA conference "windpower," Honolulu, USA, 1988.

[21] J. Van Leuven and D. Stevens, "The wind farm of Zeebrugge: Experimental set-up," J. Wind. Eng. Ind. Aerodyn. **27**, 139 (1988).

[22] S. G. Voutsinas, K. G. Rados, and A. Zervos, "On the analysis of wake effects in wind parks," J. Wind. Eng. Ind. Aerodyn. **14**, 204 (1990).

[23] N. Troldborg, G. C. Larsen, H. A. Madsen, K. S. Hansen, J. N. Sørensen, R. Mikkelsen "Numerical simulations of wake interaction between two wind turbines at various inflow conditions" Wind Energy. **14**(7), 859 (2011).

[24] U. Hassan, A. G. Glendinning, and C. A. Morgan, "A wind tunnel investigation of the wake structure and machine loads within small wind turbine farms," in *Proceedings of the 12th BWEA Wind Energy Conference*, edited by T. D. Davies, J. A. Halliday, and J. P. Palutikov (Norwich, UK, 1990), pp. 47–52.

[25] S. Frandsen, "On the wind speed reduction in the center of large clusters of wind turbines," J. Wind. Eng. Ind. Aerodyn. **39**, 251 (1992).

[26] P. B. S. Lissaman, "Energy effectiveness of arbitrary arrays of wind turbines," AIAA Paper No. 79-0114:1–7, 1979.

[27] J. D. Albertson and M. B. Parlange, "Surface length-scales and shear stress: Implications for land-atmosphere interaction over complex terrain," Water Resour. Res. **35**, 2121 (1999).

[28] S. Frandsen, R. Barthelmie, S. Pryor, O. Rathmann, S. Larsen, J. Hojstrup, and M. Thogersen, "Analytical modelling of wind speed deficit in large offshore wind farms," Wind. Energy **9**, 39 (2006).

[29] E. Bou-Zeid, C. Meneveau, and M. B. Parlange, "A scale-dependent Lagrangian dynamic model for large eddy simulation of complex turbulent flows," Phys. Fluids **17**, 025105 (2005).

[30] C.-H. Moeng, "A large-eddy simulation model for the study of planetary boundary-layer turbulence," J. Atmos. Sci. **41**, 2052 (1984).

[31] J. D. Albertson and M. B. Parlange, "Natural integration of scalar fluxes from complex terrain," Adv. Water Resour. **23**, 239 (1999).

[32] F. Porté-Agel, C. Meneveau, and M. B. Parlange, "A scale-dependent dynamic model for large-eddy simulation: Application to a neutral atmospheric boundary layer," J. Fluid Mech. **415**, 261 (2000).

[33] C. Canuto, M. Y. Hussaini, A. Quarteroni, and T. A. Zang, *Spectral Methods in Fluid Dynamics* (Springer-Verlag, New York, 1988).

[34] M. Frigo and S. G. Johnson, "The design and implementation of FFTW3," Proc. IEEE **93**, 216 (2005) (special issue on "Program Generation, Optimization, and Platform Adaptation").

[35] H. Tennekes and J. L. Lumley, *A First Course in Turbulence* (MIT, Cambridge, MA, 1972).

[36] A. Jimenez, A. Crespo, E. Migoya, and J. Garcia, "Advances in large-eddy simulation of a wind turbine wake," J. Phys.: Conf. Ser. **75**, 012041 (2007).

[37] A. Jimenez, A. Crespo, E. Migoya, and J. Garcia, "Large-eddy simulation of spectral coherence in a wind turbine wake," Environ. Res. Lett. **3**, 015004 (2008).

[38] Y.-T. Wu and F. Porté-Agel, "Large-eddy simulation of wind-turbine wakes: Evaluation of turbine parameterization," Boundary-Layer Meteorol. **138**, 345 (2011).

[39] J. Meyers and C. Meneveau, "Large eddy simulations of large wind-turbine arrays in the atmospheric boundary layer," in 48th AIAA Aerospace Sciences Meeting, Orlando, Florida, 4–7 January 2010.

[40] M. R. Raupach, R. A. Antonia, and S. Rajagopalan, "Rough-wall turbulent boundary layers," Appl. Mech. Rev. **44**, 1 (1991).

[41] H. Lu and F. Porté-Agel, "Large-eddy simulation of a very large wind farm in a stable atmospheric boundary layer," Phys. Fluids **23**, 065101 (2011)

[42] F. Porté-Agel, "A Scale-dependent dynamic model for scalar transport in large-eddy simulations of the atmospheric boundary layer," Boundary-Layer Meteorol. **112**, 81 (2004).

[43] R. Stoll and F. Porté-Agel, "Dynamic subgrid-scale models for momentum and scalar fluxes in large-eddy simulations of neutrally stratified

atmospheric boundary layers over heterogeneous terrain," Water Resour. Res. **42**, W01409 (2006).

[44]R. Stoll and F. Porté-Agel, "Surface heterogeneity effects on regional-scale fluxes in stable boundary layers: Surface temperature transitions," J. Atmos. Sci. **66**, 412 (2006).

[45]P. Moin, K. D. Squires, and S. Lee, "A dynamic subgrid-scale eddy viscosity model for compressible turbulence and scalar transport," Phys. Fluids **3**, 2746 (1991).

[46]M. Germano, U. Piomelli, P. Moin, and W. H. Cabot, "A dynamic subgrid-scale eddy viscosity model," Phys. Fluids A **3**, 1760 (1991).